Multiwavelength Observations of a Developing Cloud System: The FIRE II 26 November 1991 Case Study

J. M. INTRIERI, W. L. EBERHARD, T. UTTAL, J. A. SHAW, J. B. SNIDER, Y. HAN, AND B. W. ORR

NOAA/ERL/Environmental Technology Laboratory, Boulder, Colorado

S. Y. MATROSOV

Cooperative Institute for Research in Environmental Sciences, University of Colorado/NOAA, Boulder, Colorado

(Manuscript received 15 July 1994, in final form 15 December 1994)

ABSTRACT

Simultaneous multiwavelength measurements of a developing cloud system were obtained by NOAA Doppler lidar, Doppler radar, Fourier transform infrared interferometer, and microwave and infrared radiometers on 26 November 1991. The evolution of the cloud system is described in terms of lidar backscatter, radar reflectivity and velocity, interferometer atmospheric spectra, and radiometer brightness temperature, integrated liquid water, and water vapor paths. Utilizing the difference in wavelength between the radar and lidar, and therefore their independent sensitivity to different regions of the same cloud, the cloud top, base, depth, and multiple layer heights can be determined with better accuracy than with either instrument alone. Combining the radar, lidar, and radiometer measurements using two different techniques allows an estimation of the vertical profile of cloud microphysical properties such as particle sizes. Enhancement of lidar backscatter near zenith revealed when highly oriented ice crystals were present. The authors demonstrate that no single instrument is sufficient to accurately describe cirrus clouds and that measurements in combination can provide important details on their geometric, radiative, and microphysical properties.

1. Introduction

Over the past decade the scientific community has recognized that clouds play a crucial, yet sometimes unclear, role in weather and climate. This fact has precipitated worldwide modeling and experimental efforts to better understand the radiative and microphysical properties of clouds. Cirrus clouds in particular have been targeted in several major field campaigns such as ICE (Rasche et al. 1990) and FIRE (see *Monthly Weather Review*, Vol. 118, No. 11, 1990).

Most recently, a diverse set of observing platforms was deployed during the First International Satellite Cloud Climatology Project (ISCCP) Regional Experiment-phase II (FIRE II) in order to study cirrus cloud properties with high temporal and spatial resolution. FIRE II was conducted in Coffeyville, Kansas, from 13 November to 7 December 1991. The FIRE II strategy was to obtain coincident observations from a broad range of complementary instrumentation including satellite-, aircraft-, and ground-based, active and passive, remote and in situ sensors. As a part of the FIRE II mission, measurements were obtained by five ground-based remote sensors from NOAA's Environmental Technology Laboratory (ETL, formerly the Wave Propagation Laboratory).

Ground-based remote sensors have some advantages over air- and spaceborne instruments for observing cirrus cloud properties. For example, the high vertical and temporal resolution and the potential continuity of the datasets compensate for the limitations imposed by the fact that these measurements are made from a single site.

Combining several ground-based remote sensors of different wavelengths has the added advantage of providing details on cirrus cloud geometric, radiative, and microphysical properties in two ways: 1) by combining the measurements in a quantitative manner to infer cloud microphysical parameters such as particle sizes, concentrations, ice water contents, and optical depths and 2) by combining the mutually exclusive parts of the datasets to piece together cloud physical properties such as cloud top, base, depth, and multiple layer height information.

In this paper we present measurements from a developing cloud system observed during FIRE II by the ETL Doppler radar, Doppler lidar, Fourier Transform Infrared Radiometer (FTIR) interferometer, and microwave and infrared radiometers and we demonstrate the

Corresponding author address: Janet M. Intrieri, Environmental Research Laboratories, NOAA, 325 Broadway, Boulder, CO 80303-3328.

advantage of using multiple instruments with differing wavelengths to accurately describe clouds. This unique multiwavelength dataset chronicles a developing cloud system over a period of six hours. The cloud evolution is described in terms of lidar backscatter, radar reflectivity and radial velocities, infrared radiometer brightness temperature, FTIR atmospheric spectra, and microwave-radiometer-integrated liquid water and water vapor paths. Each instrument is described in section 2. In section 3 we present the cirrus cloud case study with the associated observations as well as combined instrument products. The results are discussed in section 4 and summarized in section 5.

2. Experiment design and instrument description

General information on the FIRE II experiment design, scientific goals, and descriptions of all the participating instruments are discussed in detail by Starr (1995). Below, we describe only the instruments used in this study. Refer to Table 1 for a comparison of specifications between the five ETL remote sensors. All of the instruments were collocated at the FIRE II hub site (latitude 37°5′50″, longitude 95°34′24″) with the exception of the radiometers and the FTIR, which were positioned 0.5 km to the northeast. The majority of data were obtained with all of the instruments pointing vertically in order to document the clouds advecting overhead and to establish continuous time series (integrated measurements) and time–height cross sections (range-gated measurements) of the cloud properties.

a. The 8.66-mm Doppler radar

The NOAA/ETL 8-mm radar (Pasqualucci and Abshire 1980) is a scanning, dual-polarization Doppler system, optimized recently for the detection of nonprecipitating cloud systems (Kropfli et al. 1994). A recent upgrade to this radar has been an offset Cassegrain antenna with reduced side lobes and improved polarization discrimination. The reduced side lobes are achieved by the minimal aperture blockage as a result of the offset antenna design.

The sensitivity of this radar can be expressed as minimum detectable reflectivity as a function of range: −51 dBZ at 1 km and −31 dBZ at 10 km. These numbers can be interpreted in terms of cloud particle size and concentrations, such that for stratus clouds 20-μm droplets in concentrations of 130 L^{-1} would be detectable at 1-km range and for cirrus clouds 50-μm diameter ice spheres in concentrations of 250 L^{-1} would be detectable at 10 km.

Cloud detection at 8-mm wavelength has some distinct advantages. For instance, compared to longer wavelength radars, the signal from ground clutter is not as strong, thereby allowing observations within 100 m or so of the radar. At the same time, 8-mm radars will readily penetrate optically thick clouds, allowing the detection of cirrus clouds that are above layers of liquid water and/or precipitation that would attenuate the signal from lidars or shorter wavelength radars.

The radar dwell times for the FIRE II project were three seconds, which represented a good compromise between improved Doppler spectral estimates without unduly increasing the Doppler spectral width. In earlier studies with the ETL 3-cm wavelength radar, the increased dwells sometimes substantially increased the detectable radar signal. For the 8-mm radar, however, the increased dwells served mainly to compress an already very large dataset.

During the FIRE II experiment, the radar operated in a zenith pointing position for 24 minutes out of every half hour and used the other six minutes of every half hour to perform Range Height Indicator (RHI) and Velocity Azimuth Display (VAD) scans. The radial resolution for all scans was 37.5 m.

b. The 10.6-μm Doppler lidar

The NOAA Doppler lidar is a mobile, pulsed, coherent, CO_2 laser radar system (Post and Cupp 1990). Although the lidar could operate on many of the numerous laser lines between 9.3 and 11.2 μm, all of the data at FIRE II were obtained at a wavelength of 10.6 μm. The lidar measures radial wind velocities in optically clear air to accuracies of about 0.5 m s^{-1} and backscattered signal intensity to ranges as great as 30

TABLE 1. ETL instrument specifications.

ETL instrument	Wavelength/frequency	Temporal/spatial averaging	Comments
CO_2 lidar	10.6 μm	1.25-s, 75.0-m range gate	Backscatter, radial velocity, .005° beamwidth
K_a-band radar	8.66 mm	3.0-s, 37.5-m range gate	Reflectivity, radial velocity, 0.8° beamwidth
Microwave radiometer	20, 31, 90 GHz	30-s, column integrated	Liquid water and water vapor, 2.5° field of view
Infrared radiometer	10.7-μm bandwidth	30-s, column integrated	Brightness temperature 2.5° field of view
Fourier transform interferometer	500–2000 cm^{-1}	1-s, atmospheric spectra	100-s averages, 2.5° field of view

km. The CO_2 lidar has some advantages over shorter-wavelength lidars for cirrus cloud studies, including eye safety at high pulse energies to detect very tenuous clouds and negligible multiple scattering that would complicate interpretation of data from all but small optical depths (Eberhard and Hardesty 1992).

Central to the transmitting system is the transversely excited atmosphere (TEA) laser in which the laser gas rapidly flows through the cavity to minimize refractive index turbulence and thus maximize laser frequency stability. Injection seeding from a continuous wave laser controls the frequency of the TEA laser pulse relative to the optical frequency reference used for Doppler measurements. The charging energy used to excite the laser gas is provided by a coronal discharge. The resulting pulse exits the pulsed TEA laser, is diverted by mirrors, and then guided out of the trailer through a computer-controlled scanner mounted on top. The frequency stability of the outgoing pulse is continuously monitored in order to ensure accurate measurements. The short-pulse mode (Eberhard et al. 1989) was used at FIRE II because of its better range resolution (60-m pulse length) compared to the more powerful long pulse.

The majority of lidar measurements were collected with the scanner pointing vertically in order to obtain extended time–height information to study the two-dimensional structure and evolution of cirrus clouds. Throughout the FIRE II dataset, the laser beam was periodically "rocked" off of vertical by as much as 10° in order to discern times when specular reflection occurred. Specular reflection can result from aerodynamically oriented hexagonal plates or columns acting as tiny mirrors that produce greatly enhanced backscatter returns when the lidar beam is pointed vertically (Eberhard and Post 1991).

Scan patterns performed by the lidar during FIRE II are similar to traditional radar scanning sequences. Occasional RHI scans were performed to reveal the more extended cloud field. Velocity accuracy deviation (VAD) scans were periodically taken to produce vertical profiles of horizontal winds using the VAD technique (Browning and Wexler 1968; Eberhard et al. 1989). The range gate length during FIRE II was 75 m, and data were usually taken at a pulse rate of 4 Hz while pointing vertically and 10 Hz while in scanning mode.

c. *Microwave and infrared radiometers*

The microwave radiometer remotely senses integrated amounts of water vapor and liquid water on a path through the atmosphere (Hogg et al. 1983). Both water vapor and liquid absorb microwave radiation and therefore produce emissions that are detected by the radiometer. These emission signals are then processed in order to retrieve the integrated amounts of liquid and vapor within the beam path. Ice, however, does not appreciably absorb at microwave wavelengths and therefore is not detected by the microwave radiometer.

The amounts of vapor and liquid are measured simultaneously but independently, using brightness temperature measurements at 20.6, 31.6, and 90.0 GHz. The total absorption at each frequency is derived from the atmospheric emission. Statistical retrieval methods are employed to derive amounts of integrated water vapor and liquid water from the total absorption. The microwave radiometer recorded data at 30-s intervals and operated with a 2.5° full angle field of view during FIRE II.

The infrared (IR) radiometer is a Barnes Model PRT-5 Radiometer modified to operate at a wavelength of 10.7 μm with a 1-μm passband. Unlike microwave radiation, IR radiation is emitted by both liquid and ice particles. The magnitude of the brightness temperature detected by the radiometer indicates the presence of clouds and the approximate cloud base temperature of optically thick clouds. The calibration for this radiometer is usually only valid for temperatures above −68°C, but the data that we show for temperatures below this have been adjusted, using a nonlinear calibration correction (Shaw et al. 1995) based on the more accurately calibrated FTIR data. Also, the detection of a cloud by the IR radiometer but not the microwave radiometer indicates the presence of ice clouds, or at least a cloud with water content below the sensitivity limit of 0.03-mm column total. The PRT-5 IR radiometer recorded data at 30-s intervals and operated with a 2.5° full angle field of view during FIRE II.

d. *Fourier Transform Infrared Radiometer*

The FTIR developed by ETL (Shaw et al. 1991) is a simple, ground-based Fourier transform interferometer similar to the ground-based instrument developed by the University of Wisconsin (Revercomb et al. 1991). It measures emission between roughly 500 and 2000 cm^{-1} with a spectral resolution variable between 1 cm^{-1} and 128 cm^{-1}. The system was operated at 1 cm^{-1} spectral resolution with a 2.5° full angle field of view during FIRE II.

The central component of the FTIR is a Michelson interferometer. Scanning the mirrors to vary the optical path difference between the beam splitter and corner-cube mirrors creates an interferogram, the Fourier transform of which is the emission power spectrum. At the input port is a beam-steering mirror that selects one of three sources: the sky, a warm blackbody simulator, and a cold blackbody simulator. The three sources are viewed sequentially and the measurements of atmospheric emission are calibrated from the measurements of the two blackbody simulators using a two-point complex calibration scheme (Revercomb et al. 1988). The two blackbody simulators are operated at near-ambient and liquid nitrogen temperatures (~300 K and 77 K) in order to bracket the expected range of equivalent brightness temperatures in atmospheric spectra.

Collection of each spectrum takes 1 second, and 100 such spectra of each source are averaged to reduce random noise. With this technique, calibrated atmospheric spectra are collected once every 10–12 minutes. During the FIRE II experiment the instrument was housed in a small unheated trailer and viewed the atmosphere through an open roof port.

3. Observations

A developing cloud system was observed on 26 November 1991 from approximately 1600 to 2200 UTC. The meteorological overview for this case is discussed in detail by Mace et al. (1995). We divide the discussion of this case study into three discrete subsets that have been determined by differences in the simultaneous lidar and radar backscatter returns as follows:

Period 1 (1610-1730 UTC). Lidar backscatter returns with no corresponding radar return. This period is characterized by high, thin, visible cirrus clouds.

Period 2 (1730-1900 and 2100-2130 UTC). Lidar and radar backscatter returns in agreement on cloud boundaries. The first part of this period is characterized by cirrus clouds, and the second part by deeper midlevel clouds.

Period 3 (1900-2100 UTC). Radar returns with corresponding lidar signal attenuation. This period is characterized by midlevel mixed phase clouds.

Measurements from all of the ETL instruments for each period are illustrated in Figs. 1, 2, and 3. Each figure corresponds to time–height cross sections of (a) the 10.6-μm lidar signal backscatter field (m^{-1} sr^{-1} in dB), (b) the 8.66-mm radar effective reflectivity factor (dBZ_e), (c) radial velocity fields (m s^{-1}), and (d) vertical air motion (m s^{-1}), which are determined from the radar radial velocities via the method described in Orr and Kropfli (1993). (Note that the lidar and radar measurements were virtually continuous, and blank areas located in between data indicate times when the radar and lidar were either in scanning mode or in between vertical and scan modes). In addition, Figs. 1–3 include time series of path-integrated values of (e) the IR radiometer (calibrated by FTIR) cloud brightness temperature (°C) and (f) the microwave radiometer liquid water (mm) and water vapor (cm) amounts. Examples of atmospheric spectra from the FTIR for each period are presented separately.

a. Period 1: 1600–1730 UTC

The skies over the experiment site were visually clear, except for contrails, at 1600 UTC and no cloud returns were received from any of the ETL instruments for several hours before this time.

The initial cirrus cloud observations were detected by the Doppler lidar at approximately 1615 UTC with the cloud base located at 10 km above ground level and cloud thickness measuring 200 m in depth (Fig. 1a). Within the ensuing 1.25 h, from the initial returns until 1730 UTC, the lidar observations showed that the cirrus cloud gradually deepens with cloud base descending to 9 km AGL and then distinguishes into two shallow layers. Toward the end of the period cloud base descended to a height of 8.8 km AGL. During this period the radar observed no cloud returns (Figs. 1b–d), except for a very brief (<1 min) period, even though thin cirrus clouds were visible by eye and documented by photographs taken from the FIRE II hub site. Note the small bump in brightness temperature at 1647 UTC, which corresponds to the only radar return during this period. This most likely resulted from an aircraft and the ensuing contrail, documented by the lidar video camera and photographs taken looking vertically from the radar at that time. The cirrus cloud had a very low emissivity value with the IR radiometer registering brightness temperatures close to that of clear-sky conditions, around −77°C (Fig. 1e). From 1615 to 1700 UTC the integrated liquid water amount was approximately 0.05 mm, which is very near the noise level of its retrieval from microwave data. The retrieved values of water vapor were approximately 1.0 cm (Fig. 1f).

A distinct feature of the lidar signal during most of this initial period was zenith-enhanced backscatter (ZEB), which is specular reflection from horizontally oriented plates (Platt et al. 1978; Thomas et al. 1990; Popov and Shefer 1994; Eberhard 1993) or possibly a similar but less pronounced enhancement from horizontally oriented columns (Eberhard 1993). Additional details of ZEB are discussed in section 4e. Figure 4 shows the lidar backscatter cross section of the cloud layer between 9.750 and 10.225 km AGL during the time period between 1718 and 1726 UTC as a function of the scanner elevation angle, which periodically dipped off zenith. An increase in density of overhead cloud and this dramatic enhancement in backscatter near zenith contributed to a 12 dB growth in cloud backscatter from 1710 to 1730 UTC. By modeling the width of the ZEB peak (Eberhard 1993; Popov and Shefer 1994) we were able to infer a lower bound of 90 μm on the average long dimension of the oriented particles for the cloud shown in Fig. 4.

In Fig. 5 two FTIR atmospheric spectra are over overlaid for comparison. The dark blue line repre-

FIG. 1. Time–height series from 1600 to 1730 UTC of (a) lidar signal backscatter (dB), (b) radar reflectivity (dBZ_e), (c) radar radial velocity (m s^{-1}), (d) corrected vertical air motion (m s^{-1}), and time series of (e) IR radiometer brightness temperature (°C), (f) microwave radiometer liquid water (mm) and water vapor (cm) integrated amounts (dashed). All heights are presented in km above ground level.

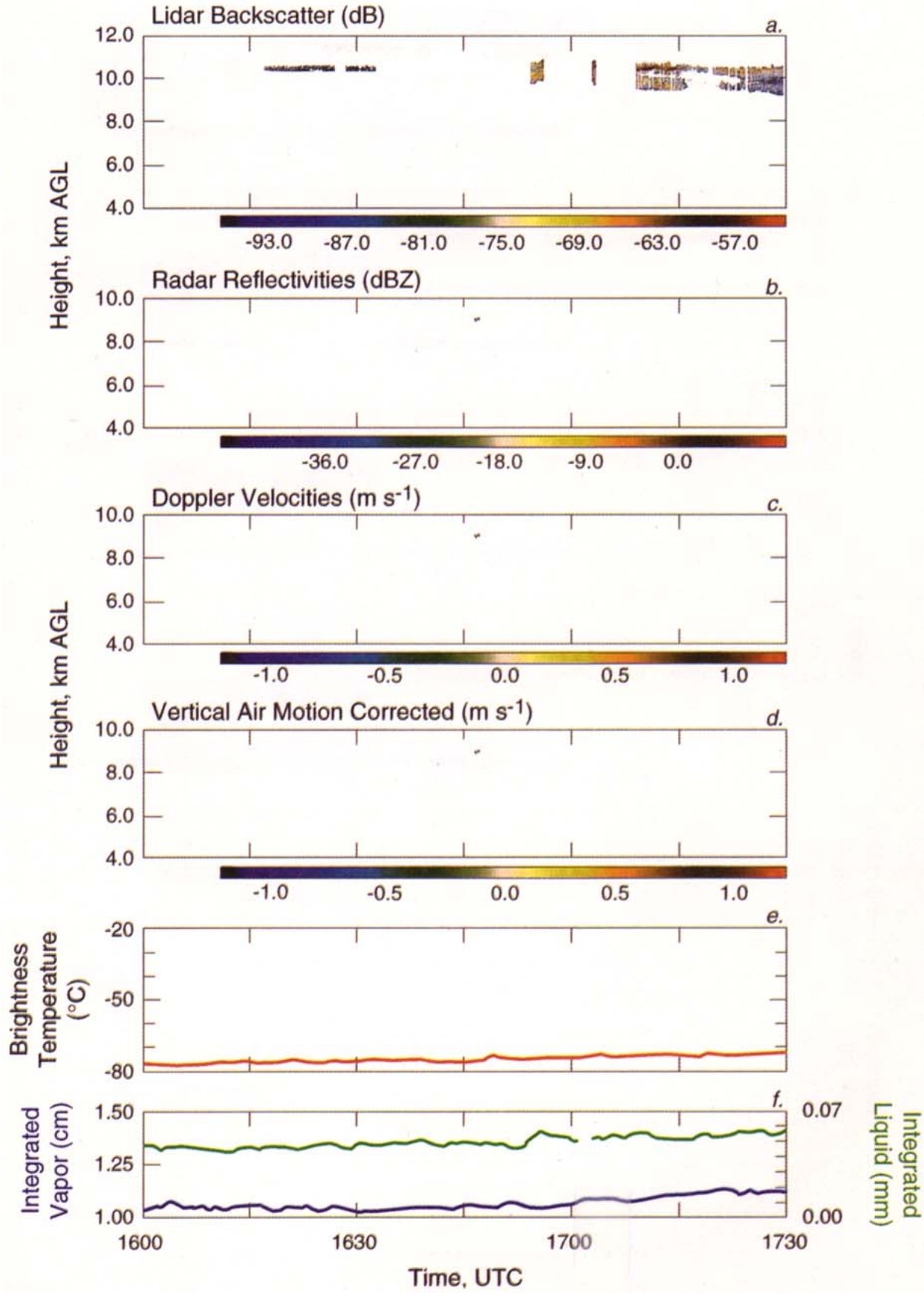
Lidar Backscatter (dB)
a.
12.0
10.0
8.0
6.0
4.0
-93.0
-87.0
-81.0
-75.0
-69.0
-63.0
-57.0
Radar Reflectivities (dBZ)
b.
10.0
8.0
6.0
4.0
-36.0
-27.0
-18.0
-9.0
0.0
Doppler Velocities (m s-1)
c.
10.0
8.0
6.0
4.0
-1.0
-0.5
0.0
0.5
1.0
Vertical Air Motion Corrected (m s-1)
d.
10.0
8.0
6.0
4.0
-1.0
-0.5
0.0
0.5
1.0
Height, km AGL
Height, km AGL
e.
Brightness Temperature (°C)
-20
-50
-80
f.
Integrated Vapor (cm)
1.50
1.25
1.00
0.07
0.00
Integrated Liquid (mm)
1600
1630
1700
1730
Time, UTC

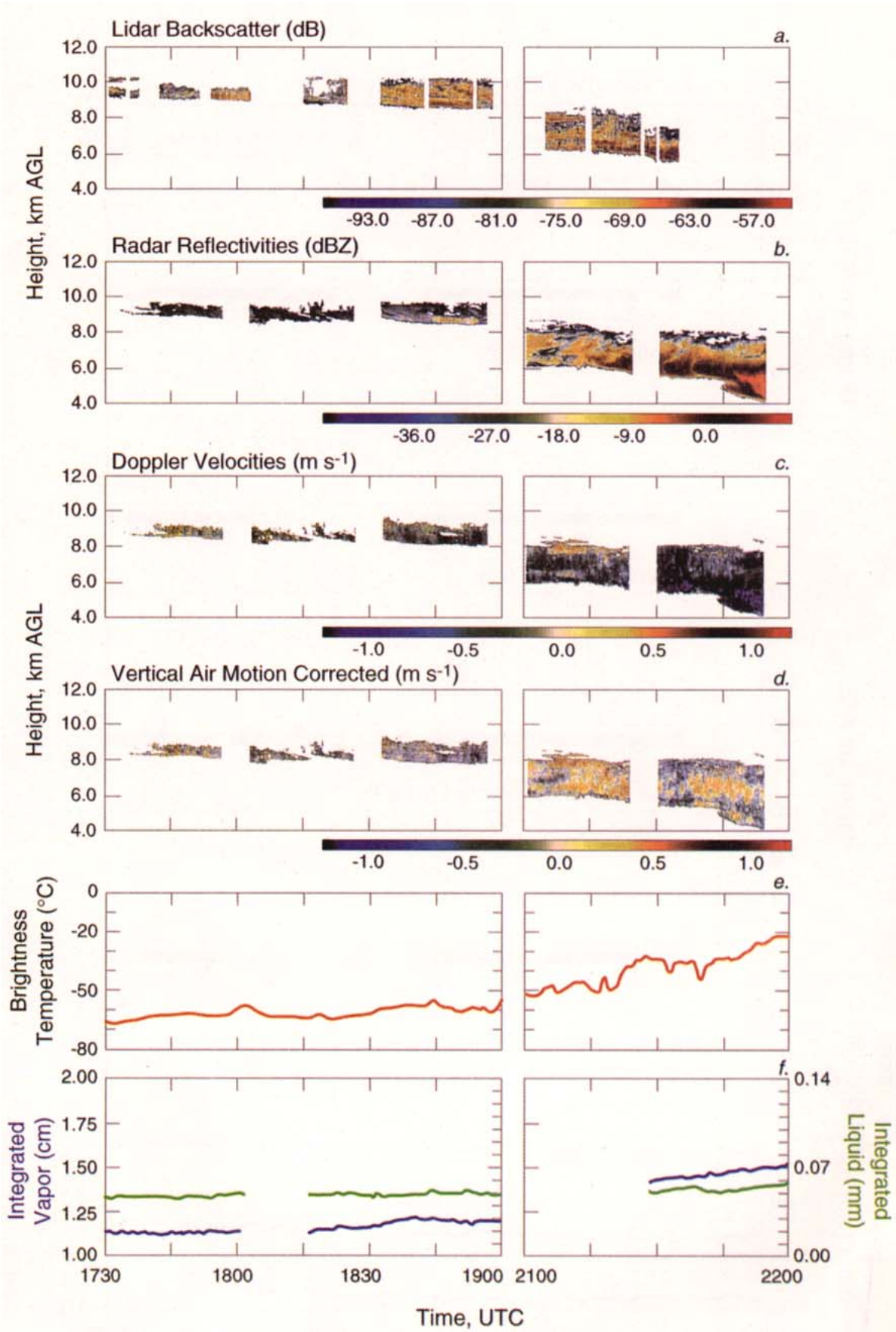

FIG. 2. As in Fig. 1 but for 1730–1900 and 2100–2200 UTC, period 2.

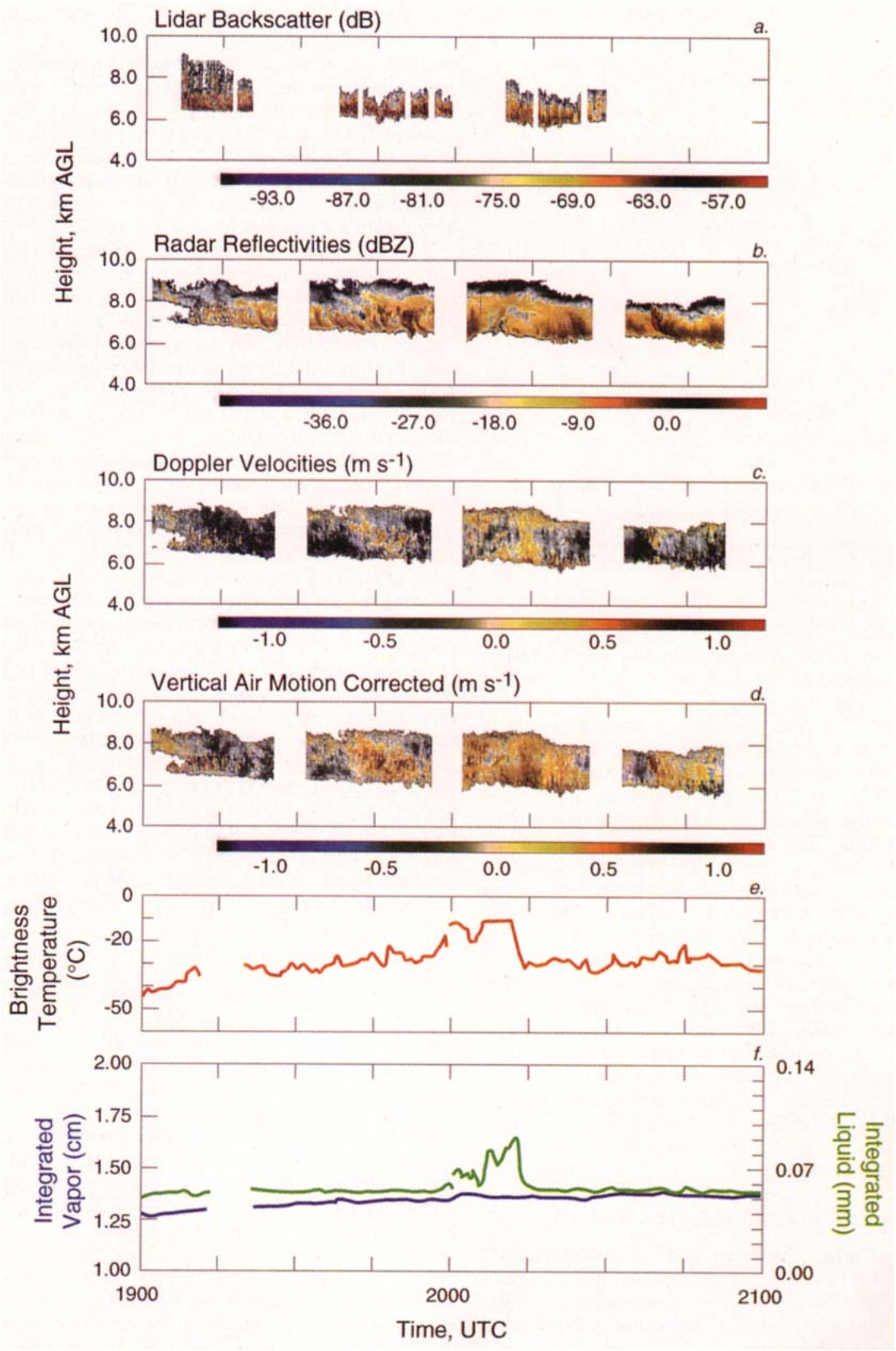

FIG. 3. As in Fig. 1 but for 1900–2100 UTC, period 3.

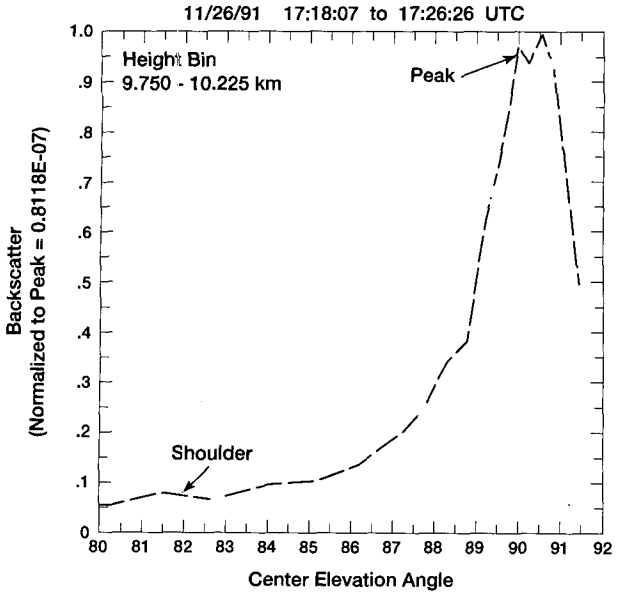

FIG. 4. Lidar backscatter cross section vs scanner elevation angle from 1718 to 1726 UTC for the cirrus cloud layer between 9.750 and 10.225 km AGL.

sents a spectrum from a cloudless period (0409 UTC) observed before the start of period 1. The red line represents the spectrum obtained during period 1 at 1709 UTC. The predominant feature to note in the clear-sky spectrum is the low and flat emission in the atmospheric window region between approximately 700 and 1300 cm^{-1}. The peak that occurs near 1050 cm^{-1} corresponds to emission from stratospheric ozone. The higher emission in the window region, as seen in the 1709 UTC profile, indicates the presence of thin cirrus clouds. Compare both spectra in the region between 600 and 700 cm^{-1} and note the difference in slope. The center of this region is sensitive to temperatures in the near region above the instrument, whereas the wings are more transparent to the lower atmospheric layer. Therefore, the shape of the curve at 0409 UTC is indicative of cooler temperatures at low levels or a temperature inversion. This is verified by a sounding launched at 0506 UTC, which is typical of a nighttime temperature profile. By 1709 UTC the inversion had eroded, and cooler temperatures were located above the warmer low-level air temperatures.

b. *Period 2: 1735–1900 and 2100–2130 UTC*

During the times between 1735 and 1900 UTC, and again from 2100 to 2130 UTC, the lidar (Fig. 2a) and radar (Figs. 2b–d) received geometrically similar cloud returns with general agreement in detected cloud top and base heights [see also Uttal et al. (1995) for a more complete discussion of cloud boundary detection using radar and lidar measurements]. Although some small differences are detected in cloud-top height, the main features of the cirrus cloud correspond very well between the two instruments (i.e., the turretlike feature between 1815 and 1825 UTC and the banded structure, indicative of fall streaks, evident throughout the time period). In some cases the radar most likely did not receive a return signal from cloud tops, which is probably due to too small or too few ice particles.

Two techniques have been developed at ETL that utilize combinations of the lidar, radar, and IR radiometer to estimate cirrus cloud particle sizes. An example from one method is shown in this section, for period 2 (combining lidar, radar, and radiometer), and the other method is shown in the following section, for period 3 (combining radar and radiometer only because the lidar signal was attenuated by cloud), to illustrate the added value of combining remote sensor measurements. We refer the readers to Matrosov et al. (1995) for an expanded discussion of both techniques and how they directly compare with each other and to in situ aircraft data. In general, both techniques compare instrument observations with theoretically expected returns to yield estimates of effective particle sizes.

Using the first technique, the lidar–radar–radiometer method described by Intrieri et al. (1993), cirrus particle sizes were estimated for the time period between 1815 and 1855 UTC and are presented in Fig. 6. Note that particles with the largest effective radii (r_e), between 80 and 90 μm, are located in three regions: 1) at cloud bottom, 2) in the generator cell or turretlike feature (1817 UTC) indicative of active cirrus cloud growth, and 3) in the ensuing fall streak feature (1820 UTC) as the cirrus begins to precipitate. Particles having the smallest sizes, between 20 and 30 μm, are located predominantly at cloud top. This cloud structure is consistent with traditional microphysical features observed in a developing cirroform cloud.

c. *Period 3: 1900–2100 UTC*

This period is marked by circumstances in which the radar observed most of or the full extent of the cloud, and the lidar signal was attenuated before reaching cloud top (Fig. 3). This period also contains the only times during this case study when liquid water was observed by the microwave radiometer.

The cloud deepened in vertical extent from approximately 1.2 to 2.4 km. In most cases the lidar signal was completely attenuated by the time it penetrated 1.25 km into the cloud (Fig. 3a). The radar reflectivity fields display a more complex vertical structure to the cloud in this growth stage, with largest reflectivities oriented in vertical bands (Fig. 3b). Also note that in the corrected vertical velocity field (Fig. 3d) there is an upward trend evident throughout the entire depth of the cloud from 2000 until 2025 UTC (warm colors indicate winds are "away" from the radar or "upward" in this figure), which coincides with the maximum in

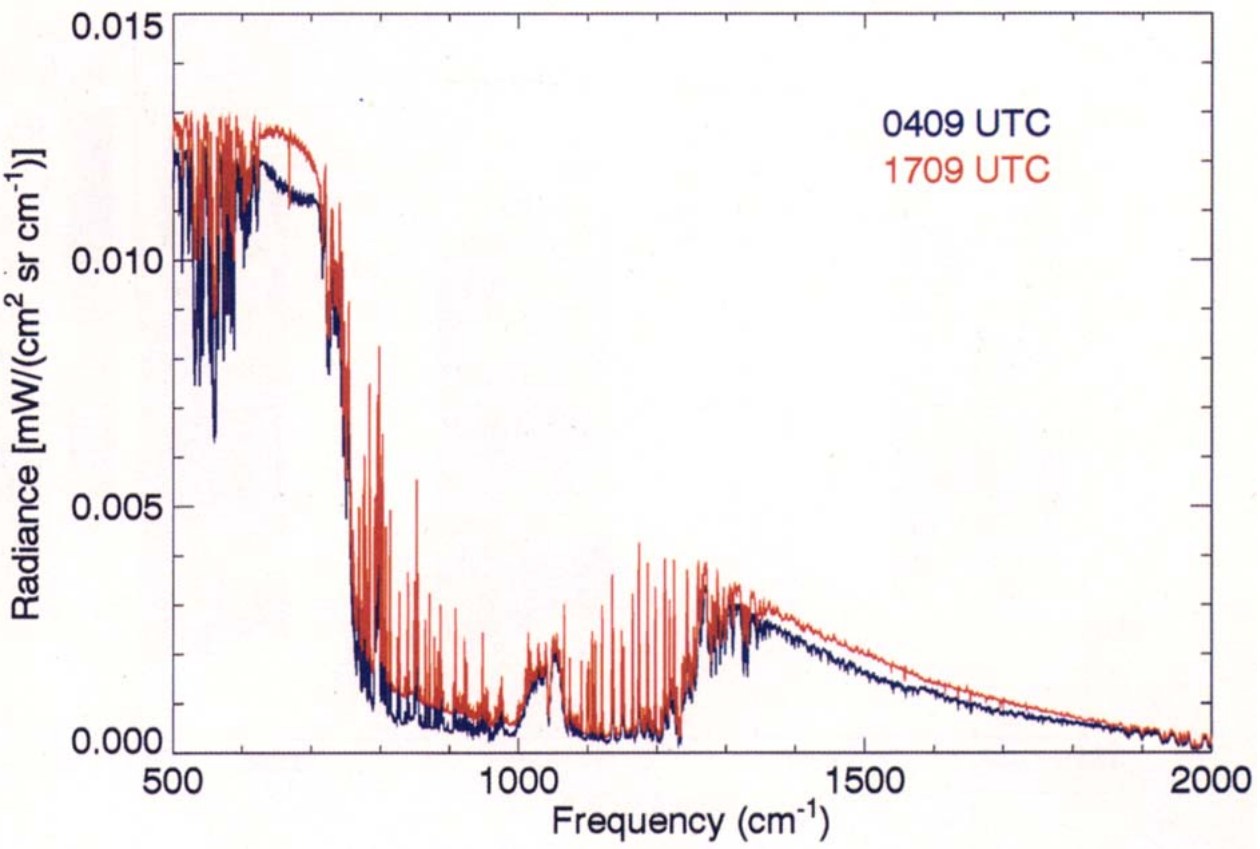

FIG. 5. FTIR atmospheric spectra for 0409 UTC (dark blue line) and 1709 UTC (red line).

liquid water and water vapor as detected by the microwave radiometer (Fig. 3e). Figure 7 shows a time–height cross section of cirrus particle median sizes derived by the second technique, the radar–radiometer method described by Matrosov et al. (1994). The size information was obtained for a time period between 2045 and 2054 UTC when the cloud was optically thick. The results are given in terms of median diameters of equal volume spheres, D_m. For the assumed distribution, $D_m \sim 2.3\ r_e$, where r_e is the effective radius of equal volume spheres; this definition of r_e is the convention used in the previous example for size retrievals. Note that the largest particles (diameter ~ 250 μm) are located in the lower region of the cloud, and the smallest-sized particles (diameter < 100 μm) are located at cloud top.

In Fig. 8, two FTIR atmospheric spectra are shown for comparison. The dark blue line represents the spectrum taken during period 2 at 1836 UTC and the red line depicts the spectrum for 1950 UTC. Compare the atmospheric window regions between these two periods and note the marked difference in slope in the 1950 UTC spectrum, which is indicative of thick cirrus and/or midlevel cloud. The ozone emission feature is predominantly damped out by 1950 UTC, indicating obscuration of the upper atmosphere by the intervening clouds.

4. Discussion

The ETL instruments contribute necessary information at different times in the evolution of this developing cloud. For example, the lidar backscatter is most sensitive to the cross-sectional area of the smaller ice particles, while the radar reflectivity is more so a measure of the mass of the larger particles in the cloud size distribution. One concern related to the interpretation of combined measurements is accounting for the difference in pulse volumes, which may introduce a bias due to the different temporal and spatial resolutions. Wherever necessary, the cloud speed and direction was accounted for and adjusted before quantitatively combining the measurements.

a. Period 1

Tenuous cirrus clouds, such as those observed during period 1, have been found to be temporally persistent and are not as seasonally or geographically variable as opaque clouds (Wylie and Menzel 1989). This subset

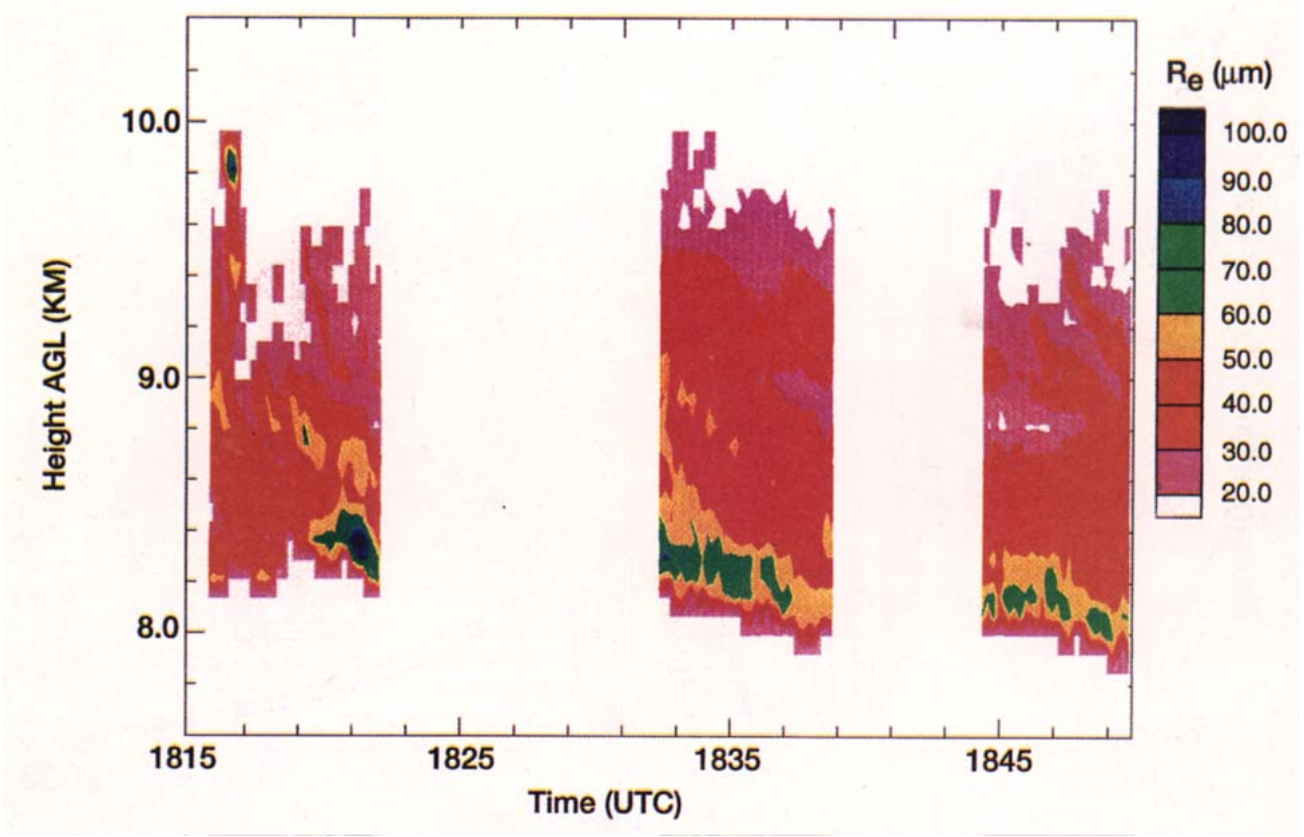

FIG. 6. Time–height cross section of effective radius (μm), calculated assuming ice spheres with a density of 0.9 g cm^{-3}, for 1815–1855 UTC, period 2.

of cirrus clouds are climatically important but not well understood or documented. Without the lidar measurements during this time period the cirrus cloud would have not been documented for 1.25 h since the radar did not register any cloud returns even though the cirrus clouds were visible to the eye. The PRT-5, without correction, detected a net signal of only 7°C, the difference between the clear-sky signal of −80°C (0409 UTC) and the signal from increased water vapor and thin cirrus cloud of −73°C (1709 UTC). Incorporating the cold-calibration correction (based on the FTIR data as mentioned in section 2c.) produced a 14°C net signal shown in Fig. 1e, the difference between −91°C at 0409 UTC and −77°C at 1709 UTC. In general, the downwelling radiative signal of these clouds at the surface was very small at IR wavelengths. This cirrus cloud may have had a significant shortwave albedo, however, owing to the high altitude position and small ice crystal dimensions at cloud top (~90 μm) coupled with the occurrence of oriented particle habit as detected by the lidar ZEB. These early cirrus clouds formed at tropopause heights (10.3 km AGL) at a depth of approximately 200 m; subsequently, they deepened with time via cloud-base lowering to a height of 9 km AGL.

b. Period 2

Although this time period exhibited two very different cloud types, namely high-altitude cirrus and high- to midlevel mixed-phase clouds, both the lidar and radar showed good agreement on cloud boundaries. Thus, it is difficult to categorically define situations when the lidar or radar cloud detection is optimum.

In the first half of this time period, the cirrus cloud exhibited very typical characteristics with generating cell and fallstreak structure as it developed from 700 m in depth to approximately 1.6 km in depth with the midcloud located at approximately 9.5 km AGL. The increase in brightness temperature detected at the surface corresponded to cloud amount depths greater than 900 m coupled with cloud base lowering. The amount of liquid water in the cloud as measured by the microwave radiometer remained constant at 0.06 mm. Cloud particle effective radii ranged from 20 to 80 μm with the median particle radius occurring at approximately 43 μm.

In the second part of this time period the brightness temperature at the surface increased markedly (−17°C) as the cloud depth approached 4.0 km and cloud-base

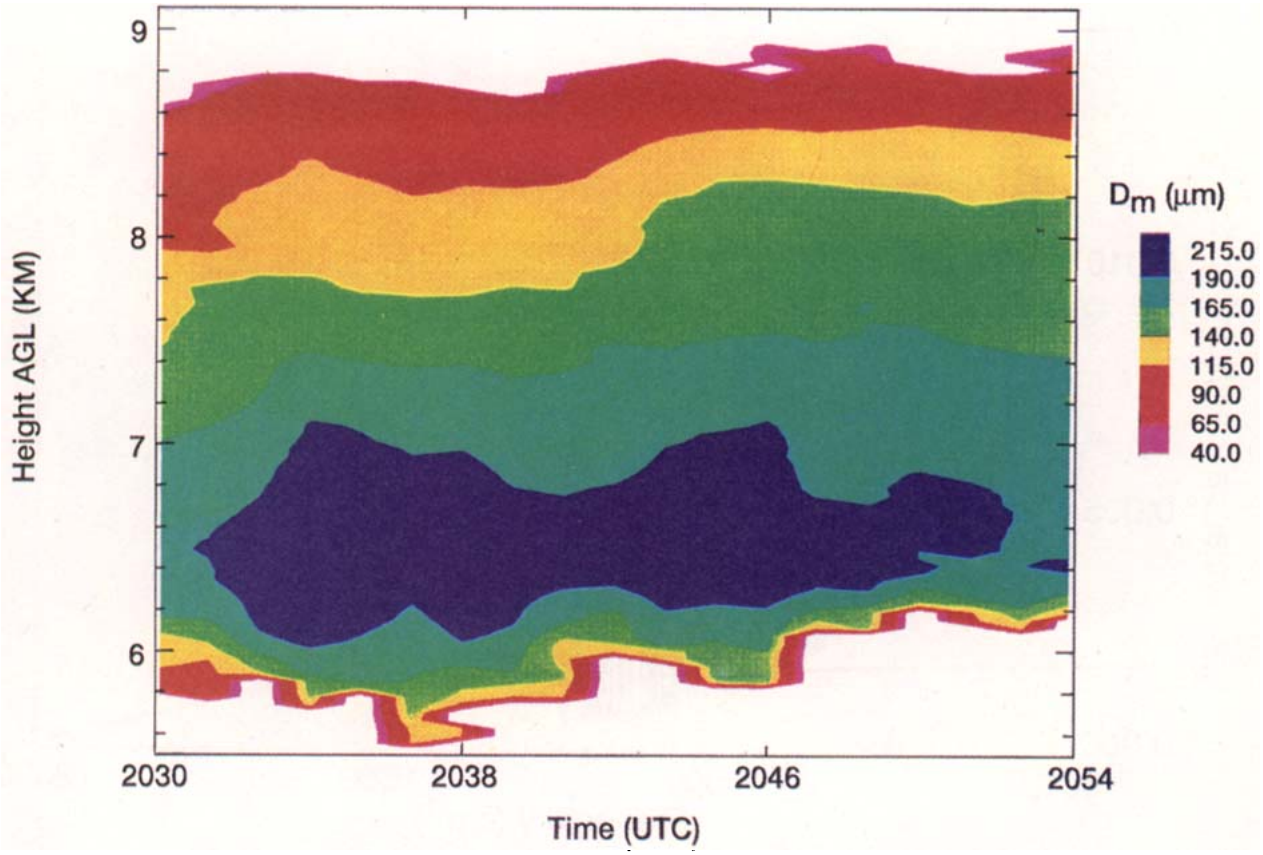

FIG. 7. Time–height cross section of median diameter (μm), calculated assuming ice spheres with a density of 0.9 g cm^{-3}, for 2045–2054 UTC, period 3.

height lowered to approximately 4.0 km AGL. The integrated cloud vapor increased from 1.35 to 1.65 cm, and the integrated cloud liquid water remained fairly constant at 0.7 mm. Precipitation was observed at the surface shortly after 2200 UTC at which time the lidar stopped taking measurements.

c. *Period 3*

In this time period the radar observed most or all of the vertical extent of the cloud to document the cloud-top heights, whereas the lidar signal became attenuated after penetrating ~1.25 km into the cloud. In general, the lidar did not penetrate through the cloud in circumstances where liquid water was detected and/or the IR extinction optical depths exceeded 1.8 and therefore would have falsely determined cloud top.

The cloud consisted of a combination of high- to midlevel clouds spanning 2.2 km in depth and producing the maximum amount of cloud liquid water (0.12 mm). Cloud particles were within the range from 70 to 250 μm in diameter with the largest particles located in the middle to lower portion of the cloud and the smallest particles at cloud top. The cloud exhibited the highest brightness temperatures (−15°C), the maximum amount of cloud liquid water (0.12 mm), and peak upward vertical motions (0.5 m s^{-1}) of any time throughout the case study.

d. *Cloud boundary detection*

A complete description of cloud boundary statistics encompassing data from the ETL radar and lidar are presented for the entire FIRE II experiment in Uttal et al. (1995). Here, we present a comparison of cloud top and base heights detected by the radar and lidar for the time period between 1800 and 2130 UTC to illustrate the importance of using both instruments for determining cloud boundaries (Uttal and Intrieri 1993).

The scatter plots in Figs. 9a and 9b show the lidar- versus radar-detected cloud base and top heights, respectively. Note that the lidar and radar had good agreement on cloud bases with the lidar sometimes detecting higher cloud bases (Fig. 9a). This is due to the lidars' collimated pencil beam detecting the finer small-scale cloud base height variations that are smoothed by the radars' large pulse volume.

Figure 9b illustrates the differences between the lidar- and radar-detected cloud-top heights. A significant number of points lie above the 1 to 1 regression line,

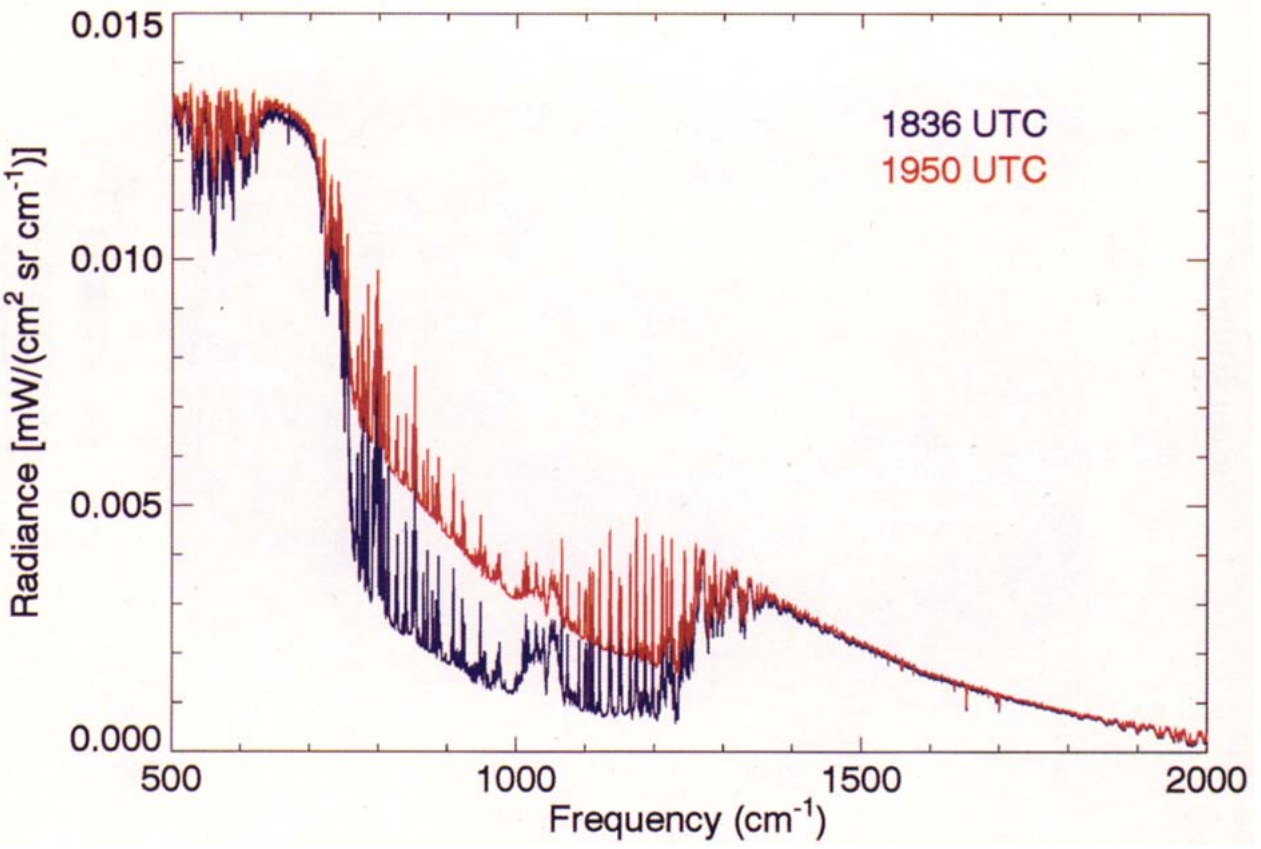

FIG. 8. FTIR atmospheric spectrum for 1836 UTC (dark blue line) and 1950 UTC (red line).

indicating lidar detecting cloud top higher than the radar. This is mainly attributed to the lidar detecting very small particles at cloud top as in period 2, in addition to detecting thin cirrus cloud not visible to the radar as in period 1. Points below the regression line are indicative of times when the lidar signal was attenuated and thereby sensing lower cloud top than detected by the radar as was the case in period 3.

In general, there is good agreement of cloud-base height determination between the lidar and radar, and the largest departures occur in cloud-top heights, which is mainly a function of the difference in wavelength between two instruments. Either the particles are too small and of too low concentration for the radar to detect or the clouds are too optically thick for the lidar signal to penetrate. In some cases the lidar detects an entire cloud layer invisible to the radar, and in a scenario not illustrated by this case study, the radar detects cirrus cloud above low-level water clouds where the lidar signal becomes completely attenuated.

e. ZEB statistics

When a hexagonal plate crystal becomes oriented with the flat side horizontal, it acts much like a partially reflecting mirror. Lidar backscatter from oriented plates is much stronger when pointed at zenith (perpendicular to the plate face) than several degrees off zenith (Platt et al. 1978; Thomas et al. 1990; Popov and Shefer 1994). Eberhard (1993) has also shown that columns or needles that are oriented with the long axis horizontal also cause ZEB, at least for a CO_2 lidar, but with much smaller peak to shoulder ratio than for plates. An understanding of ZEB is important when interpreting lidar backscatter data. The radiative properties of a cloud also depend partly on crystal orientation because the geometrical cross section of the particles when horizontally oriented is larger for the vertical direction than when randomly oriented.

ZEB does provide some information about the oriented particles. When the peak to shoulder ratio is much larger than possible for columnar crystals, a large fraction of the particles can be presumed to be oriented plates. For smaller peak to shoulder ratio the ZEB information alone is ambiguous because the cloud may contain a large percentage of columns, a small percentage of plates, or both, with the remainder of the particles randomly oriented. For perfectly oriented crystals the angular width of the ZEB peak, which is determined partly by diffraction, is proportional to wavelength and inversely proportional to the particle's long dimension (Eberhard 1993; Popov and Shefer

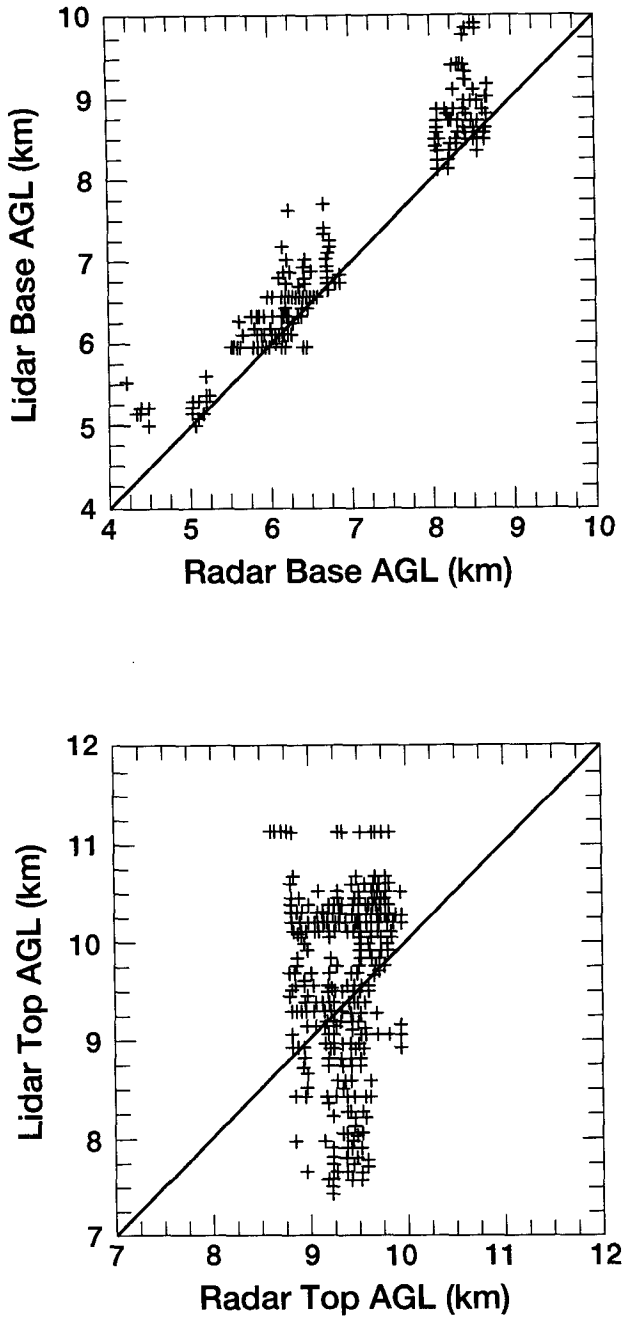

FIG. 9. Cloud boundary scatterplot for (a) lidar cloud-base vs radar cloud-base and (b) lidar cloud-top vs radar cloud-top heights for 1800–2130 UTC.

1994). However, flutter or crystal imperfections may cause a distribution of orientations near horizontal, which also widens the ZEB peak (Platt et al. 1978; Popov and Shefer 1994). The width of the ZEB peak thus provides a lower bound on the average long dimension of the oriented particles.

Figure 10 shows the statistics of the strength of the ZEB signature for the CO_2 lidar between 1657 and 2151 UTC, comprising a total of 112 minutes of near-zenith scanning, or 38% of this period. These data include both high and middle clouds. ZEB was detected to some degree in about 80% of the observed clouds, whereas Thomas et al. (1990) reported ZEB in half of the clouds in their more comprehensive dataset. The peak to shoulder ratio in Fig. 10 was negligible (<1.25, or 1 dB) for 14% of the clouds. Strong attenuation by lower clouds or patchiness of the observed layer made recognition of ZEB unclear for about 7% of the observed clouds. The peak to shoulder ratio was modest (1.25–4, or 1–6 dB) for about 50% of the clouds. A strong ZEB peak to shoulder ratio (>16, or 12 dB) was present in 10% of the clouds, and the highest peak to shoulder ratio reached 300, or 25 dB. ZEB varied in time at all heights but was more prominent in the higher clouds observed in periods 1 and 2 than in the midlevel clouds that dominated period 3.

5. Summary

Results from a FIRE II cirrus cloud case study are presented to illustrate the advantages of multiwavelength observations. The combination of measurements from the Environmental Technology Laboratory's ground-based lidar, radar, interferometer, and radiometers yield two-dimensional geometrical, microphysical, and radiative information not attainable by any one of these instruments alone.

We have shown examples of multiple instrument products, including cirrus cloud top and base heights from combined radar and lidar backscatter measurements and vertical profiles of microphysical properties, such as particle sizes, which can be estimated from both the radar–radiometer and lidar–radar–radiometer combinations.

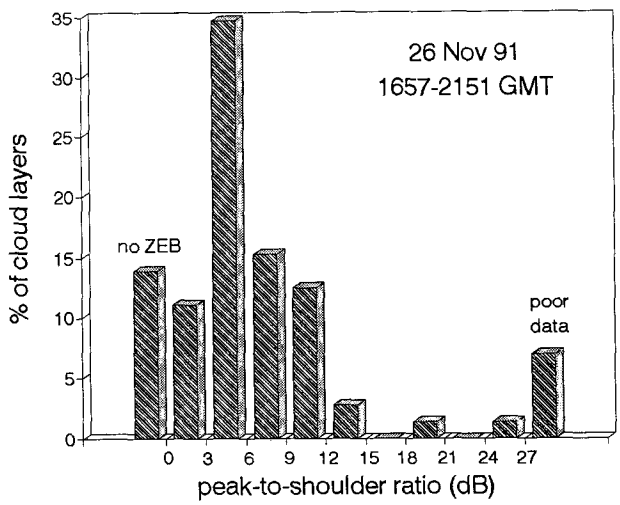

FIG. 10. Histogram of lidar ZEB statistics for 1600–2130 UTC.

The PRT-5 infrared radiometer by itself qualitatively indicated an increase in water vapor and cirrus clouds, but a correction based on the more sensitive and better-calibrated FTIR was necessary to provide accurate brightness temperatures of the tenuous cirrus. The FTIR radiances can also be combined with the radar and lidar backscatter, with many advantages over the PRT-5 including a larger bandwidth, better calibration, and much higher spectral resolution (Matrosov et al. 1993). In addition, the FTIR measurements can be used to invert lower-level vertical profiles of atmospheric temperature and water vapor (Smith et al. 1991). In combination with cloud information from the lidar and radar, these profiles can be extended through the atmosphere to the base of the cloud.

Other ETL combined instrument measurements and applications are highlighted in separate papers in this issue, including quantitative information from the present case study which was not reiterated here; for example, cloud boundary (see Baum et al. 1995) and cloud microphysical information (see Young et al. 1994) for satellite validation, comparisons between other ground-based remote sensing techniques (see Collard et al. 1995), and cloud boundary statistics (see Uttal et al. 1995).

We are currently in the process of relating the effects and relative importance of cirrus cloud properties such as particle size, concentration, ice water path, and depth, to the amount of IR radiation received at the surface. With the addition of temperature information from radiosonde data, we have the capability to evaluate and contribute to previously established empirical relationships, which have been based on limited amounts of data. We are also continuing our efforts to investigate other meaningful products that can be derived from combinations of multiple instrument datasets for additional cloud parameters, as well as for other cloud types and conditions, such as clouds in the tropical and polar regions. With the addition of new ETL instruments operating at different wavelengths (i.e., 2-μm and ozone lidars) since the FIRE II experiment was performed, we have a continuing opportunity to explore other combined instrument techniques.

Acknowledgments. The authors gratefully acknowledge the work and dedication in the field of all those who maintained and operated the ETL instruments, especially R. Willis, R. Cupp, M. J. Post, C. Grund, M. Hardesty, L. Olivier, B. Martner, J. Gibson, B. Bartram, K. Clark, M. Jacobsen, and B. Madsen. We are also grateful to everyone back in the laboratory who helped with computer support and data processing, especially K. Healy, E. Ash, A. Keane, B. Stankov, R. Beeler, and A. Francavilla. This research was sponsored by the NOAA Climate and Global Change Program and by DOE Grant DE-FG02-90ER61059 in the Atmospheric Radiation Measurement Program.

REFERENCES

Baum, B. A., T. Uttal, M. Poellet, T. P. Ackerman, J. M. Alvarez, J. M. Intrieri, D. O'C. Starr, J. Titlow, V. Tovinkere, and E. Clothiaux, 1995: Satellite remote sensing of multiple cloud layers. *J. Atmos. Sci.*, **52,** 4210–4230.

Browning, K. A., and R. Wexler, 1968: The determination of kinematic properties of a wind field using Doppler radar. *J. Appl. Meteor.*, **7,** 105–113.

Collard, A. D., S. A. Ackerman, W. L. Smith, X. Ma, H. E. Revercomb, R. O. Knuteson, and S.-C. Lee, 1995: Cirrus cloud properties derived from high spectral resolution infrared spectrometry during FIRE II. Part III: Ground-based HIS results. *J. Atmos. Sci.*, **52,** 4264–4275.

Eberhard, W. L., 1993: Cirrus properties deduced from CO_2 lidar observations of zenith-enhanced backscatter from oriented particles. FIRE Cirrus Science Results 1993. NASA Conf. Publ. 3238, 63–66.

——, and M. J. Post, 1991: CO_2 lidar techniques for observing characteristic particle size of selected cloud types. Preprints, *Lower Tropospheric Profiling: Needs and Technologies,* Boulder, CO, Amer. Meteor. Soc., 7–8.

——, and R. M. Hardesty, 1992: Coherent CO_2 lidar: A superior system for observing clouds? NASA Conf. Publ. 3158, 501–504.

——, R. E. Cupp, and K. R. Healy, 1989: Doppler lidar measurements of profiles of turbulence and momentum flux. *J. Atmos. Oceanic Technol.*, **6,** 809–819.

Hogg, D. C., M. T. Decker, F. O. Guirard, K. B. Earnshaw, D. A. Merritt, K. P. Moran, W. B. Sweezy, R. G. Strauch, E. R. Westwater, and C. G. Little, 1983: A steerable dual-channel microwave radiometer for measurement of water vapor and liquid in the troposphere. *J. Climate Appl. Meteor.*, **22,** 789–806.

Intrieri, J. M., G. L. Stephens, W. L. Eberhard, and T. Uttal, 1993: A method for determining cirrus cloud particle sizes using a lidar and radar backscatter technique. *J. Appl. Meteor.*, **32,** 1074–1082.

Kropfli, R. A., S. Y. Matrosov, T. Uttal, B. W. Orr, A. S. Frisch, K. A. Clark, B. W. Bartram, and J. B. Snider, 1994: Studies of cloud microphysics with millimeter wave radar. *Atmos. Res.*, in press.

Mace, G. G., D. O'C. Starr, T. P. Ackerman, and P. Minnis, 1995: Examination of coupling between an upper-tropospheric cloud system and synoptic-scale dynamics diagnosed from wind profiler and radiosonde data. *J. Atmos. Sci.*, **52,** 4094–4127.

Matrosov, S. Y., T. Uttal, J. B. Snider, and R. A. Kropfli, 1992: Estimation of ice cloud parameters from ground-based infrared radiometer and radar measurements. *J. Geophys. Res.*, **97,** 11 567–11 574.

——, D. K. Lynch, and J. H. Churnside, 1993: Possibilities of using IR spectrometer data for sizing cirrus cloud particles. *Proc., Passive Infrared Remote Sensing of Clouds and the Atmosphere.* Orlando, FL, Soc. Opt. Eng., 381–387.

——, B. W. Orr, R. A. Kropfli, and J. B. Snider, 1994: Retrieval of vertical profiles of cirrus cloud microphysical parameters from Doppler radar and infrared radiometer measurements. *J. Appl. Meteor.*, **33,** 617–626.

——, A. J. Heymsfield, J. M. Intrieri, B. W. Orr, and J. A. Snider, 1995: Ground-based remote sensing of cloud particle sizes during the 26 November 1991 FIRE II cirrus case: Comparison with in situ data. *J. Atmos. Sci.*, **52,** 4128–4142.

Orr, B. W., and R. A. Kropfli, 1993: Estimation of cirrus cloud particle fall speeds from vertically pointing Doppler radar. Preprints, *26th Int. Conf. on Radar Meteorology,* Norman, OK, Amer. Meteor. Soc., 588–590.

Pasqualucci, L., and N. L. Abshire, 1980: A comparison of cloud top and cloud base measurements by lidar and 8.6-mm radar. Preprints, *19th Conf. on Radar Meteorology,* Miami Beach, FL, Amer. Meteor. Soc., 718–721.

Platt, C. M. R., N. L. Abshire, and G. T. McNice, 1978: Some microphysical properties of an ice cloud from lidar observation of horizontally oriented ice crystals. *J. Appl. Meteor.*, **17,** 1220–1224.

Popov, A. A., and O. V. Shefer, 1994: Theoretical and numerical investigations of the intensity of the lidar signal specular reflected from a set of oriented ice plates. *Appl. Opt.*, **33,** 7038–7044.

Post, M. J., and R. E. Cupp, 1990: Optimizing a pulsed Doppler lidar. *Appl. Opt.*, **29,** 4145–4158.

Rasche, E., D. Hennings, R. Sefzig, and M. Quante, 1990: International Cirrus Experiment: Field Phase Plan. Institut für Geophysik und Meteorologie, Universität zu Köln, 129 pp.

Revercomb, H. E., H. Buijs, H. B. Howell, D. D. LaPorte, W. L. Smith, and L. A. Sromovsky, 1988: A radiometric calibration of the IR Fourier transform spectrometers: Solution to a problem with the High-Resolution Interferometer Sounder. *Appl. Opt.*, **27,** 3210–3218.

——, F. A. Best, R. G. Dedecker, T. P. Dirkx, R. A. Herbsleb, R. O. Knuteson, J. F. Short, and W. L. Smith, 1991: High spectral resolution Fourier transform infrared (FTIR) instruments for the atmospheric radiation measurement program: Focus on the atmospheric emitted radiance interferometer. *Proc. of Second Atmospheric Radiation Measurement Science Team Meeting,* Denver, CO, 121–125.

Shaw, J. A., J. H. Churnside, and E. R. Westwater, 1991: An infrared spectrometer for ground-based profiling of atmospheric temperature and humidity. *Proc. SPIE Int. Symp. on Optical Applied Science and Engineering,* San Diego, CA, Society of Photo-Optical Instrumentation Engineers, 681–686.

——, J. B. Snider, J. H. Churnside, and M. D. Jacobson, 1995: Comparison of infrared atmospheric brightness temperatures measured by a Fourier Transform spectrometer and a filter radiometer. *J. Atmos. Oceanic Technol.*, **12,** 1124–1128.

Smith, W. L., H. M. Woolf, and R. E. Revercomb, 1991: Linear simultaneous solution for temperature and absorbing constituent profiles from radiance spectra. *Appl. Opt.*, **30,** 1117–1123.

Thomas, L., J. C. Cartwright, and D. P. Waring, 1990: Lidar observations of horizontal orientation of crystals in cirrus clouds. *Tellus,* **42B,** 211–216.

Uttal, T., and J. M. Intrieri, 1993: Comparison of cloud boundaries measured with 8.6 mm radar and 10.6 μm lidar. *Proc., Combined Optical-Microwave Earth and Atmosphere Sensing,* Albuquerque, NM, IEEE, 207–210.

——, ——, W. L. Eberhard, T. P. Ackerman, and E. Clothiaux, 1995: Cloud boundaries during FIRE II. *J. Atmos. Sci.,* **52,** 4276–4284.

Wylie, D. P., and W. P. Menzel, 1989: Two years of cloud cover statistics using VAS. *J. Climate,* **2,** 380–392.

Young, D. F., S. Mayor, P. Minnis, J. M. Intrieri, S. Y. Matrosov, and J. B. Snider, 1994: Comparison of satellite and surface-based remote sensing of cloud microphysical properties during FIRE cirrus phase II. Preprints, *Eighth Conf. on Atmospheric Radiation,* Nashville, TN, Amer. Meteor. Soc., 231–233.